

Article

Adsorptive Capacity, Inhibitory Activity and Processing Techniques for a Copper-MOF Based on the 3,4-Dihydroxybenzoate Ligand

Estitxu Echenique-Errandonea ¹, Sara Rojas ², Víctor Karim Abdelkader-Fernández ², Manuel Pérez-Mendoza ², Ricardo F. Mendes ³, Paula Barbosa ⁴, Filipe Figueiredo ⁴, Flávio Figueira ³, Filipe A. Almeida Paz ³, José Manuel Delgado-López ², Antonio Rodríguez-Diéguez ^{2,*} and José Manuel Seco ^{1,*}

¹ Departamento de Química Aplicada, Facultad de Química, Universidad del País Vasco UPV/EHU, Paseo Manuel Lardizabal, N° 3, 20018 Donostia-San Sebastián, Spain

² Departamento de Química Inorgánica, Facultad de Ciencias, Universidad de Granada, Av. Fuentenueva S/N, 18071 Granada, Spain

³ Department of Chemistry, CICECO—Aveiro Institute of Materials, University of Aveiro, 3810-193 Aveiro, Portugal

⁴ Department of Materials & Ceramic Engineering, CICECO—Aveiro Institute of Materials, University of Aveiro, 3810-193 Aveiro, Portugal

* Correspondence: antonio5@ugr.es (A.R.-D.); josemanuel.seco@ehu.eus (J.M.S.)



Citation: Echenique-Errandonea, E.; Rojas, S.; Abdelkader-Fernández, V.K.; Pérez-Mendoza, M.; Mendes, R.F.; Barbosa, P.; Figueiredo, F.; Figueira, F.; Almeida Paz, F.A.; Delgado-López, J.M.; et al. Adsorptive Capacity, Inhibitory Activity and Processing Techniques for a Copper-MOF Based on the 3,4-Dihydroxybenzoate Ligand. *Molecules* **2022**, *27*, 8073. <https://doi.org/10.3390/molecules27228073>

Academic Editor: Athanassios C. Tsipis

Received: 23 October 2022

Accepted: 11 November 2022

Published: 21 November 2022

Publisher's Note: MDPI stays neutral with regard to jurisdictional claims in published maps and institutional affiliations.



Copyright: © 2022 by the authors. Licensee MDPI, Basel, Switzerland. This article is an open access article distributed under the terms and conditions of the Creative Commons Attribution (CC BY) license (<https://creativecommons.org/licenses/by/4.0/>).

Abstract: Due to the fast, emerging development of antibiotic-resistant bacteria, the need for novel, efficient routes to battle these pathogens is crucial; in this scenario, metal-organic frameworks (MOFs) are promising materials for combating them effectively. Herein, a novel Cu-MOF—namely **1**—that displays the formula $[\text{Cu}_3\text{L}_2(\text{DMF})_2]_n$ (DMF = *N,N*-dimethylformamide) is described, synthesized by the combination of copper(II) and 3,4-dihydroxybenzoic acid (H_3L)—both having well-known antibacterial properties. The resulting three-dimensional structure motivated us to study the antibacterial activity, adsorptive capacity and processability of the MOF in the form of pellets and membranes as a proof-of-concept to evaluate its future application in devices.

Keywords: metal-organic frameworks; material processing; adsorption capacity; antibacterial activity

1. Introduction

Infections caused by pathogenic bacteria have been considered one of the most concerning global threats affecting public healthcare. To tackle this problem, over the years, antibiotics have been administered to treat bacterial infections. However, due to the growing resistance of pathogens to conventional antibiotics, treatments often become less effective or even ineffective. Consequently, the need to develop new effective solutions to broaden the range of antibacterial agents and combat infections more efficiently has become very important [1,2].

In this context, coordination chemistry offers a great alternative in the design of new bioactive compounds [3,4]. In particular, our research group has worked with such materials in fields as diverse as diabetes [5], cancer [6], Alzheimer's [7], inflammatory processes [8], Chagas disease and leishmaniasis [9]. In recent years, metal-organic frameworks (MOFs) have been presented as promising materials for the treatment and detection of disease-related conditions. Bacterial activity in MOFs can be conducted by two other mechanisms [2,10]: In the most common mechanism, MOFs act as reservoirs of bioactive metal ions and their gradual degradation leads to a controlled release, resulting in a sustained antibacterial effect with high efficiency. The other mechanism supports the theory that antibacterial activity results from interactions between the bacterial surface and the active site of MOF's surface. In this latter case, active centres present in MOFs are stabilised by

strong chemical bonds in such a way that the material maintains its robustness and keeps its structure, but is weak enough not to block antibacterial activity [11].

In the former described mechanism, antibacterial properties stem not only from the release of bioactive metal ions but also from the organic linkers, giving rise to a combined synergetic antibacterial effect in the media. Another critical factor in promoting its antibacterial properties is the particle size of the MOF [12]; decreasing its particle size to the nanoscale range results in a considerable enhancement of the surface area, allowing for a greater numbers of interactions with its surrounding, and even prompting its internalisation into the cells.

The multifunctional characteristics of copper make it an ideal candidate for application in fields as wide as from catalysis to adsorption [4,13]. Cu^{2+} has recognised antifouling, antifungal and antibacterial properties; it is also relatively affordable, abundant and well-known for eradicating bacterial infections [14–17]. It has been widely used in clinics in particular, where multiple applications of copper-based sterilising materials have been found [1,11].

Among the copper-based MOF materials—for example, HKUST-1 and MOF-199—many have been extensively studied in the field of bactericidal materials due to their simple synthetic route and the low toxicity of their ligands [18]. Several approaches for immobilising MOFs into various substrates have been carried out over the last few years with the idea of developing new materials with promising properties [2,19]. The application spectrum is broad: from textiles that could be used as wound dressings that inhibit bleeding and promote healing, to coatings that prevent bacterial adhesion to surfaces to avoid biofilm formation [19]. In this line, Rodríguez et al. [11,20] reported the immobilisation of Cu-BTC on cellulose fibres, exhibiting good antibacterial activity for *Escherichia coli* (*E. coli*) [20]. The immobilisation was performed by exposing cellulosic substrates to Cu-BTC MOF precursors to achieve in situ synthesis of the material in a basic media. The antibacterial activity, in this case, arises from gradual degradation and Cu^{2+} liberation, inducing damage to the bacterial envelope [21].

Another possible shaping and immobilising procedure can be packing MOFs into pellets, monoliths or membranes. As MOFs generally yield insoluble and non-dense products, they tend to display problems when incorporated into devices as they can blow off and contaminate pipes easily in charge/discharge cycles. Thus, bulk-material processing has become a mandatory procedure for implementing MOFs in the industry. The selection of the shaping technique depends on the textural properties of the chosen material. Generally, the shaped material must keep or enhance its mechanical strength and it must be a simple and cost-effective procedure [22,23].

Even though shaping and processing MOFs for specific applications is still at an early stage, efforts are dedicated to bringing MOFs towards real-world applications [24–27]. Thus, apart from shaping, it has become mandatory to test processed materials under the humidity, applied-pressure conditions and high operating temperatures that can be encountered in industrial processes. In this line, Figueira et al. [28] reported a work where they presented a simple and inexpensive method for immobilising MOFs in the form of pellets and membranes and studied the stability of processed materials in terms of their resistance to different temperatures and humidity to simulate possible industrial operating conditions. They performed these studies in Cu-BTC and MOF-74 MOFs, motivated by the well-known capacity of these materials to adsorb harmful gases such as CO_2 and due to the possible competition of ambient water molecules with the gases that are supposed to be captured in the porous network [29].

In this work, we report a novel three-dimensional copper-based MOF composed of the bioactive 3,4-dihydroxybenzoic acid ligand. The structure displays the formula $[\text{Cu}_3\text{L}_2(\text{DMF})_2]_n$, (1), where H_3L corresponds to the organic linker. Considering the antibacterial activity of Cu^{2+} ions and that the organic linker composing the MOF—which exhibits well-known performance against pathogenic bacteria [30]—1's antibacterial activity has been studied and compared with the free ligand and Cu^{2+} as controls. Additionally,

following the immobilisation approach of the material reported by Figueira et al. [28], **1** has been shaped into pellets and membranes, and its behaviour under different thermal and moisture conditions has been studied in processed materials. Additionally, the microporous structure of **1** enabled us to test the CO₂ adsorption of the material following the Yang et al. [29] strategy, where the surface area and CO₂ adsorption of Cu-BTC was improved via a solvent-exchange procedure.

2. Results and Discussion

2.1. Crystal Structure Details

Compound **1** was further analysed by single-crystal X-ray crystallography and its structure unveiled was as [Cu₃L₂(DMF)₂]_n·(DMF = *N,N*-dimethylformamide); **1** crystallized in the centrosymmetric space group *C2/c* with an asymmetric unit composed of 1.5 Cu²⁺ cations (half of the Cu²⁺ is located in an inversion point), a L^{3−} organic linker and a highly disordered DMF molecule (Figure 1).

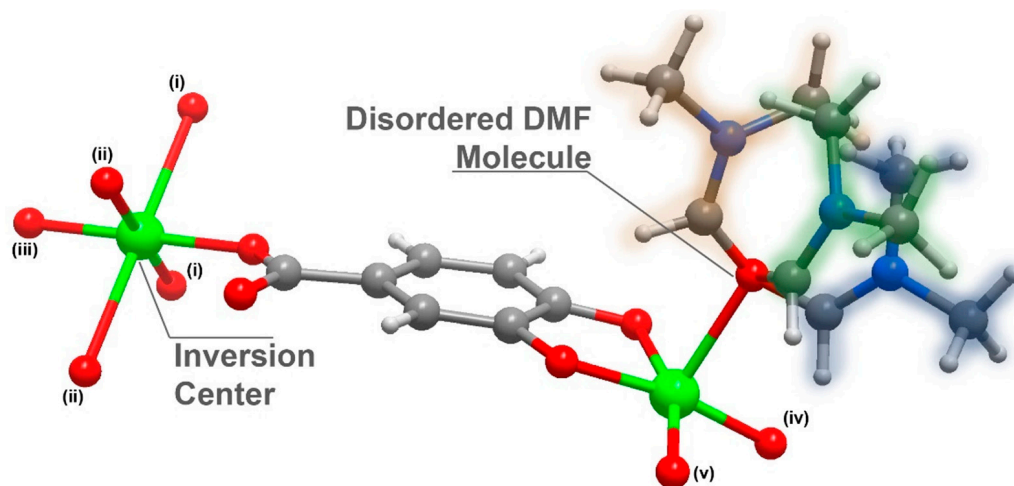


Figure 1. Schematic representation of the asymmetric unit in [Cu₃L₂(DMF)₂]_n (**1**), emphasizing the disorder present in the coordinated DMF molecule and the inversion centre present in the Cu2 atom. Metal centre coordination environments were generated using the symmetry transformation (i) $x + 3/2, y + 1/2, -z + 1/2$; (ii) $x + 1/2, -y + 3/2, z + 1/2$; (iii) $-x + 2, -y + 2, -z + 1$; (iv) $x - 1/2, -y + 3/2, z - 1/2$; (v) $-x + 1, y, -z + 1/2$.

The organic linker 3,4-dihydroxybenzoate was fully deprotonated and showed coordination to the metallic centre, both from the carboxylate moiety as well as from the phenoxide groups. The oxygens in the carboxylic group coordinated to two metal centres in a simple $\kappa^{-1}\text{-O}$ coordination mode, while the oxygens from the phenoxide groups coordinated in a $\mu_2\text{-O,O}$ and $\kappa^{-2}\text{-O}$ coordination mode, coordinating to three metal centres. The Cu1 atom displayed a penta-coordinated environment ($\{\text{CuO}_5\}$, Figure 2a) being linked to three ligands and a DMF molecule. Concretely, the CuO₅ environment was composed of the coordination of two phenoxide moieties of one ligand (one oxygen worked as a bridge between two neighbouring Cu1 centres and the other between a Cu1 and a Cu2 centre) and an additional phenoxide moiety that corresponded to another linker molecule (which also connected two Cu1 metals, with $d_{\text{Cu1}\dots\text{Cu1}} = 3.0125(2)$ Å), as well as the coordination of one donor atom belonging to the carboxylate moiety of another ligand molecule. The surrounding of Cu1 was completed by coordinating an additional oxygen atom belonging to a DMF solvent molecule, which acted as a direct bridge between a Cu1 and a Cu2 meta centre.

Cu₂, instead presents with a hexa-coordinated environment ($\{\text{CuO}_6\}$, Figure 2a), being linked to four ligands and two symmetry-related DMF molecules. When the CuO₆ surrounding was examined in detail, two of the oxygen atoms belonged to phenoxide moieties of two distinct linker molecules, which acted as a nexus between the Cu1 and Cu2 centres

($d_{\text{Cu1}\dots\text{Cu2}} = 3.0459(2) \text{ \AA}$), in addition to the coordination of another two oxygen donor atoms belonging to a carboxylate moiety of two symmetry-related linkers. The coordination sphere was then completed by two oxygen atoms from the DMF molecules. Continuous shape measurements (CShMs) [31] revealed that the Cu1 and Cu2 atoms built different polyhedra, with Cu1 and Cu2 resembling a square pyramid (SPY-5) and octahedron polyhedra (OC-6), respectively (see Tables S1 and S2 for more detailed information).

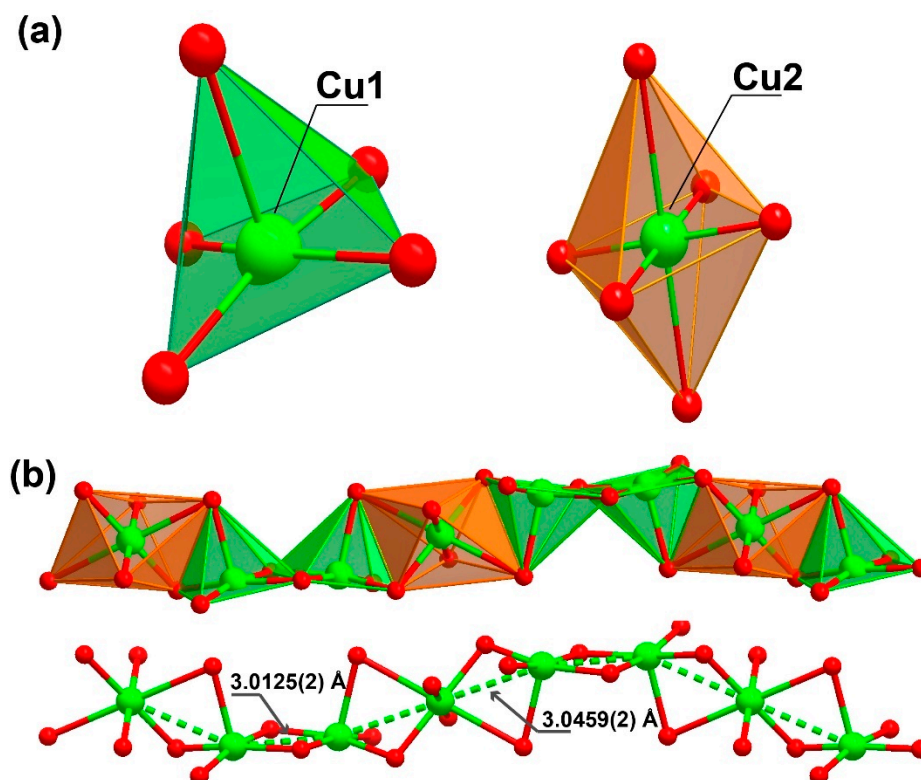


Figure 2. Representation of the (a) coordination environment present for the two crystallographically independent Cu^{2+} cations, exhibiting a square pyramid and a octahedral coordination sphere (for Cu1 and Cu2, respectively) and (b) the inorganic chain with a “ABBA” connectivity between the metal centres extending along the (011) plane present in $[\text{Cu}_3\text{L}_2(\text{DMF})_2]_n$ (**1**).

This high level of coordination led to the formation of an inorganic chain extending along the (011) plane (Figure 2b). Taking into account the connectivity achieved among these SBUs, it may be considered an “ABBABBA” model, considering A as Cu2 and B as Cu1. These inorganic chains are in turn “connected” by the organic linker, forming a porous 3D structure (Figures 3 and S1).

Considering the connectivity of all the metals and ligands, the resulting structure possessed a previously non-described topology (Figure 3) that can be simplified by the $(4^2 \cdot 8^2 \cdot 10^2)(4^3)_2(4^4 \cdot 6^3 \cdot 8^3)_2$ point symbol [32]. The growth of this structure along the *c* axis left narrow microchannels that were occupied by disordered DMF molecules displaying a pointing-out disposition in the pores and taking advantage of the whole pore cavity; thus, no solvent-accessible volume was left according to the geometrical calculations performed with the PLATON-v1.18 program [33]. This is also supported by the thermogravimetric analysis (TGA) and X-ray performed (Figures S2–S5).

2.2. Processing into Pellets and Membranes

Following the approach of Figueira et al., [28] the bulk material was processed into pellets and membranes to explore simple and cost-effective processing techniques [28]. A homemade extrusion system allowed for the compression of **1**, forming a pellet; for the purpose of supporting cohesion to the bulk material, water was employed as a binding agent.

The aforementioned procedures are described in detail in the Supplementary Material. With the materials shaped, moisture and temperature stability studies were carried out and the stability of the processed material was determined by powder X-ray diffraction (PXRD).

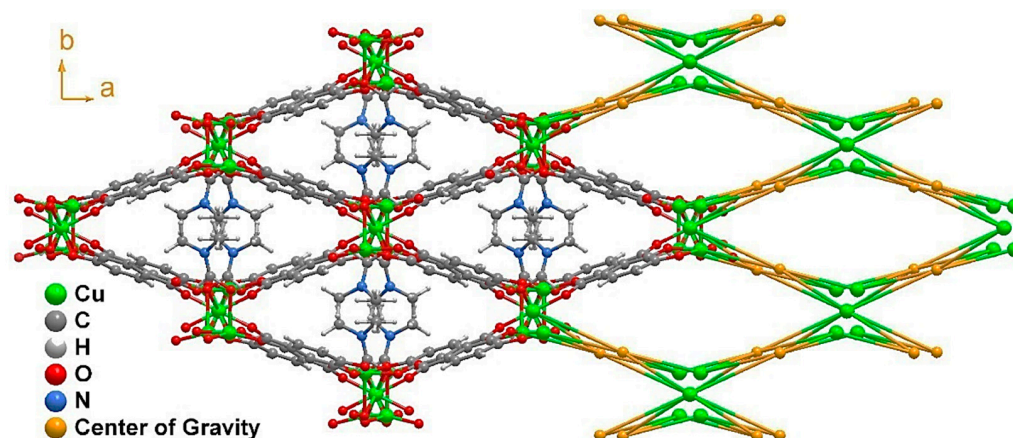


Figure 3. Structural packing of $[\text{Cu}_3\text{L}_2(\text{DMF})_2]_n$ (**1**) as viewed in the (001) direction, alongside its topological view. The disorder present in the DMF molecule was removed for clarity.

2.3. Moisture Stability

The powder X-ray diffraction patterning performed in **1** demonstrated that the pristine MOF, as well as the shaped materials (pellets and membranes), kept its stability under high relative humidity (98% RH) conditions for 72 h. In the case of the membrane-immobilised material of **1**, despite the amorphous nature of the polysulphone (PSF) polymeric matrix, the reflexions from **1** were still present and well-defined. The PXRD results (Figure S6) show that compound **1** was stable and kept its structure after being processed into pellets or membranes and being exposed for 72 h to 98% RH. Nonetheless, in the additional tests related to the solvent-exchange procedure (where we examine the material's stability upon being submerged in methanol, ethanol and water), we appreciated that when the material (**1**) was in direct contact with water, it evolved into another crystalline phase; however, prolonged exposure to humidity did not provoke a material transformation and it remained stable.

2.4. Temperature Stability

After performing humidity tests, the pellets were tested against temperature cycles. Four heating and cooling-down cycles (from 125 °C to room temperature—RT) were conducted and the shaped materials were characterised by PXRD analysis. A photograph taken after each cycle gave an idea of the integrity of the pellet (Figure S7). After the second and fourth cycles, PXRD analyses were conducted in coated and uncoated pellets. Coated and uncoated pellets of **1** exhibited excellent resistance to humidity and subsequent temperature-cycles, maintaining the pellet's integrity and not suffering from humidity-derived structural transformation. Nonetheless, it must be admitted that coated pellets kept their integrity better as the resistance was supported by the polymer.

2.5. Adsorption Studies

2.5.1. Water Adsorption

Water-vapour adsorption isotherms were measured at 25 °C in the bulk of **1** to ascertain the amount of water adsorbed at different relative humidities (2–98%). According to the results, the as-synthesised (AS) compound **1** presented with a very low variation in mass change—precisely 1.5%—which could be indicative of monolayer-type adsorption in the surface of the MOF. Nonetheless, when the solvent-exchange procedure was carried out (stirring 100 mg of compound **1** in 4 mL of EtOH for 16 h) by thermogravimetric analysis (TG) and PXRD, it was deduced that the material remained stable and it appeared that the

coordinated DMF molecules were replaced by EtOH molecules (see Figure S8 for more detailed information). In agreement with this, the water adsorption isotherm showed a three-times higher mass change than the as-synthesised compound **1**, exhibiting an uptake of 6%. However, compound **1** exhibited low uptake even after the solvent-exchange procedure, which could be due to the hydrophobic character of the MOF.

2.5.2. Gas Adsorption Capacity

Subsequently, to assess Cu-MOF porosity, we studied its adsorption capacity toward gases. First, we performed adsorption isotherm studies on the as-synthesised material **1** towards N₂ and CO₂ adsorbates at 77 K and 273 K, respectively, after an outgassing step at 170 °C for 6 h (Figure S9). Regarding N₂ adsorption, Cu-MOF loaded 7.9 cm³/g (0.4 mmol/g) at the maximum relative pressure ($P/P_0 = 1$). This low N₂ uptake capacity resulted in a low surface area value, 4 m²/g—characteristic of non-porous materials—as calculated using the Brunauer–Emmett–Teller (BET) equation. Focusing on CO₂ adsorption, its load was also low, barely surpassing 5 cm³/g (0.2 mmol/g) at a relative pressure of 0.03.

Considering the relatively low uptake for N₂ and CO₂, we decided to proceed with the solvent exchange procedure as it was performed for the water-adsorption studies. Similarly, compound **1** was suspended in ethanol for 16 h, and the sorption studies were repeated. In the latter case, sample outgassing was performed for the as-synthesised material, and the adsorption capacity was evaluated for N₂ at 77 K and CO₂ at 273 K (Figure 4). Under the conditions mentioned earlier, **1** exhibited a 2.5-fold increased maximum N₂ loading of 20 cm³/g (0.9 mmol/g), indicating that the solvent exchange strategy had a positive, although limited, effect on its mesoporosity. This was reflected in its overall surface area, as the BET surface almost quadrupled from 4 m²/g to 15 m²/g.

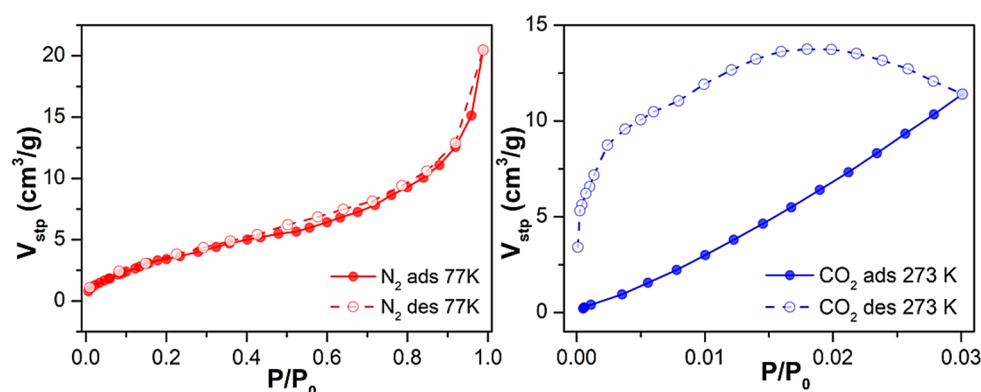


Figure 4. N₂ and CO₂ adsorption and desorption isotherms at 77 K and 273 K of **1** upon outgassing at 170 °C for 6 h after solvent exchange with EtOH.

Regarding CO₂ uptake, adsorption in the micropores increased (up to 11 cm³/g at $P/P_0 = 0.03$, corresponding to 0.5 mmol/g), exhibiting—according to the Dubinin–Astakhov equation—a micropore volume of 0.5 cm³/g, significantly larger than the 0.15 cm³/g displayed by the as-synthesised material. The obtained results are comparable and in line with work reported in the literature so far [34–36]. It can be highlighted that in the work of Güçlü et al. they reported a family of transition metal and oxalamide-functionalized-based MOFs displaying CO₂ adsorption; in particular, the Cd-OATA MOF exhibited 0.51 mmol/g adsorption at 298 K.

2.6. Antibacterial Activity

The inhibitory activity of the samples was assessed against pathogenic gram-positive *Staphylococcus aureus* (*S. aureus* bacteria), which causes a wide variety of clinical diseases [37]; the results are shown in Figure 5. Copper nitrate, H₃L and compound **1** inhibited the bacteria's growth in a media that was favourable for the growth of the pathogen. Table 1 shows the area of inhibition generated around each of the solid samples after 24 h incubation.

As can be observed, both samples—the copper salt and compound 1, which contained a similar mass of Cu (Table 1)—exhibited practically the same area of inhibition. Thus, *S. aureus* pathogenic growth can likely be inhibited upon MOF dissolution and subsequent Cu^{2+} release, which further diffuses through the agar; the ligand's release can also partially inhibit its growth. These results suggest that the inhibitory activity of Cu and the ligand remained practically unaltered after the formation of the MOF.

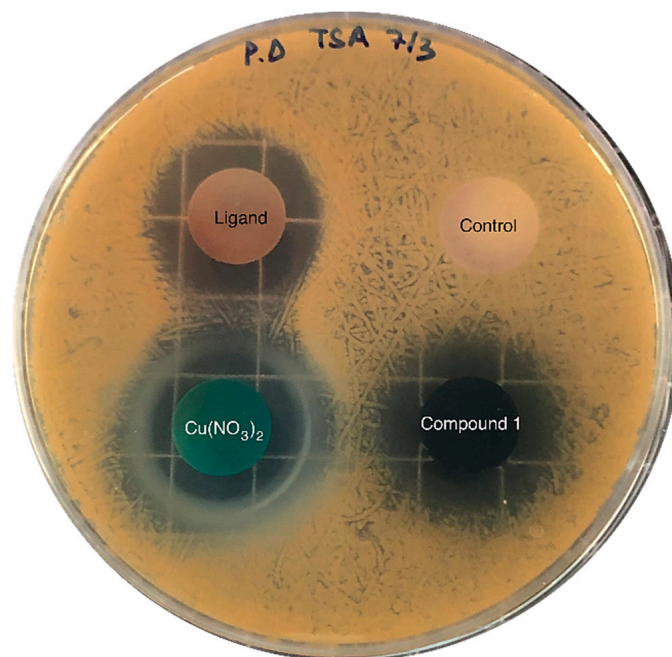


Figure 5. Diffusion assays showing the inhibitory activity against *S. aureus* of copper nitrate, H_3L (ligand) and compound 1. The negative control sample—without inhibitory activity—contained calcium phosphate, which was also used as a supporting material in the rest of the samples (25 mg of active compound and 75 mg of calcium phosphate).

Table 1. Area of inhibition (cm^2) of the compound against *S. aureus*. Values are shown as mean \pm standard deviation (SD, $n = 3$). The mass of Cu and H_3L in each sample is also provided.

Compound	Inhibition Area (cm^2)	Mass of Cu (mg)	Mass of Ligand (mg)
H_3L	3.6 ± 0.3	-	25
$\text{Cu}(\text{NO}_3)_2$	4.2 ± 1.7	6.8	-
Compound 1	4.1 ± 0.8	6.9	10.7

The reported results are in line with the work reported by Lee et al. [38], where they investigated the antibacterial activity derived from NO-releasing Cu-BTC by the disk diffusion method in six bacterial strains. Regarding the obtained results for the *S. Aureus* Gram-positive strain, the inhibition area was $414.2 \pm 18.4 \text{ mm}^2$ for Cu-BTC and $376.8 \pm 21.6 \text{ mm}^2$ for NO-Cu-BTC.

3. Materials and Methods

3.1. Preparation of Complexes

All chemicals were reagent grade and were used as obtained.

Synthesis of $[\text{Cu}_3\text{L}_2(\text{DMF})_2]_n$

- General procedure for synthesising single crystals: 0.010 g (0.065 mmol) of 3,4-dihydroxybenzoic acid (L) organic linker was dissolved in 0.5 mL of DMF. In a separate vial, 0.010 g (0.0434 mmol) of $\text{Cu}(\text{NO}_3)_2 \cdot 2.5\text{H}_2\text{O}$ was dissolved in 0.5 mL of distilled

water. After the ligand and metal dissolution, 0.5 mL of H₂O was added to the ligand solution and 0.5 mL of DMF to the metal solution. The metal solution was added dropwise to the ligand solution with magnetic stirring. The resulting greenish-turquoise solution was poured into a screw-capped vial (6 mL) and introduced to the oven at 95 °C for 6 h, giving rise to dark-brown ribbon-shaped single crystals. Single-crystal X-ray structure determination, FT-IR (Figure S10), elemental analysis (EA; Table S3) confirmed the general formula [CuL₂(DMF)₂]_n.

- General procedure for the scale-up synthesis: 0.2 g (1.2 mmol) of 3,4-dihydroxybenzoic acid ligand and 0.2 g (0.868 mmol) of Cu(NO₃)₂·2.5H₂O were weighed and dissolved in 3 mL DMF/3 mL H₂O solvent mixture. This greenish-turquoise solution was placed in a microwave and heated at 95 °C for an hour to obtain around 85 mg of Cu MOF (yielding ~75%). PXRD confirmed the purity of the product. Data related to the EA, FTIR and TG can be found in the Supplementary Material. SEM images of compound 1 are shown in Figure S11.

3.2. X-ray Diffraction Data Collection and Structure Determination

Details of the structure determination and refinement of compound 1 are summarised in Tables 2 and S4. Crystallographic data for the structures reported in this paper have been deposited with the Cambridge Crystallographic Data Center as a supplementary publication—CCDC 2195988. Power X-ray diffraction is shown in Figure S12. Moreover, compound 1 stability was examined in various solvents (Figure S13).

Table 2. Crystallographic data and structure refinement details of compound 1.

Compound	1
Formula	C ₁₀ H ₁₀ Cu _{1.50} NO ₅
Formula weight	319.50
Temperature/K	150 (2)
Crystal system	Monoclinic
Space group	C2/c
<i>a</i> /Å	20.2893 (16)
<i>b</i> /Å	8.6194 (7)
<i>c</i> /Å	16.7337 (11)
<i>α</i> /°	90.0
<i>β</i> /°	126.632 (2)
<i>γ</i> /°	90.0
Volume/Å ³	2348.4 (3)
<i>Z</i>	8
<i>μ</i> (Mo Kα)/mm ^{−1}	2.75
Crystal type	Red plate
Crystal size/mm	0.16 × 0.14 × 0.06
<i>θ</i> range (°)	3.42–25.35
Index ranges	−24 ≤ <i>h</i> ≤ 22 −10 ≤ <i>k</i> ≤ 10 −20 ≤ <i>l</i> ≤ 20
Collected Reflections	17154
Independent Reflections	2141 (<i>R</i> _{int} = 0.023)
Completeness to <i>θ</i> = 25.24	99.6%
Final <i>R</i> indices [<i>I</i> > 2σ(<i>I</i>)]	<i>R</i> 1 = 0.0354 <i>wR</i> 2 = 0.0964
Final <i>R</i> indices (all data)	<i>R</i> 1 = 0.0386 <i>wR</i> 2 = 0.0984
Largest diff. peak and hole /eÅ ^{−3}	0.66 and −0.99

$$^a R1 = \frac{\sum ||F_o| - |F_c||}{\sum |F_o|}, ^b wR2 = \sqrt{\frac{\sum [w(F_o^2 - F_c^2)^2]}{\sum [w(F_o^2)^2]}}, ^c w = 1 / [\sigma^2(F_o^2) + (mP)^2 + nP] \text{ where } P = (F_o^2 + 2F_c^2)/3.$$

3.3. Inhibitory Activity against *Staphylococcus Aureus* (*S. aureus*)

The pathogenic strains of *Staphylococcus Aureus* (CECT 976, *S. aureus*) were supplied by the Colección Española de Cultivos Tipo (CECT). The pathogenic strain was grown in tryptic soy broth (TSB No2, Sigma-Aldrich) at 30 °C, following the supplier's recommendations.

The inhibitory activity of copper nitrate, the ligand and compound **1** was evaluated by agar diffusion assays. This assay was carried out as follows: 0.1 mL of an overnight culture of *S. aureus* was spread on Petri dishes containing TSA (containing 3 % *v/v* of TSB and 1.5% *w/v* agar). Then, pellets of each sample were placed on agar plates containing the pathogenic bacteria and incubated at 30 °C—the pathogen's optimal temperature. After 24 h of incubation, the inhibition zones were imaged and compared. Pellets of 100 mg were prepared by mixing 75 mg of calcium phosphate and 25 mg of the sample (copper nitrate, the ligand or compound **1**, respectively) and then pressed using a compact hydraulic press at 10 tons. A 100 mg calcium phosphate pellet was also prepared and analysed as a negative control. Inhibition experiments were performed in triplicate. The inhibition area was measured with ImageJ software; it was obtained by subtracting the area of the pellet from the total area. Data are shown as mean values and the corresponding standard deviation (SD).

3.4. Material Shaping: Processing into Pellets and Membranes

Pellets: 100 mg of compound **1** was weighed and 100 µL of water was added to yield a malleable paste. Afterwards, the paste was transferred into a syringe and compressed by applying heat to eliminate excess binding agent. For increased endurance, pellets of **1** were submerged for 2 s in a solution containing 300 mg of polysulphone (PSF) in CH₂Cl₂. Solvent evaporation gave place to a pellet of **1** covered by a transparent film of PSF.

Membranes: Compound **1** was also immobilised in polymeric membranes. This material was shaped according to the following procedure: 400 mg of polysulphone (PSF) was weighed and dissolved in 5 mL of dichloromethane (CH₂Cl₂). To this dense solution, 100 mg of compound **1** were added and stirred for 30 min. The remaining viscous solution was then cast in a glass petri dish and left unstirred at ambient conditions until the complete evaporation of the solvents. Note that the membrane preparation conditions were optimised through essays containing various MOF-to-polymer ratios to achieve a balanced coverage homogeneity and mechanical stability.

3.5. Pellet and Membrane Moisture Stability Tests

After compound **1** was shaped into pellets and membranes, the stability of these processed materials was examined against possible operating industrial conditions such as moisture and temperature cycles. So, first, pellets and membranes of **1** were treated for 72 h in a desiccator containing a K₂SO₄-saturated solution, which simulated 98% relative humidity (RH) [39]; subsequently, the moisture stability was checked. Afterwards, pellets were treated with temperature cycles. In all cases, the stability of the processed material was determined by PXRD.

4. Conclusions

We have synthesised a novel copper MOF based on 3,4-dihydroxybenzoic acid as a ligand shaped by a simple and non-expensive processing method. Furthermore, we checked the shaped material's stability by means of temperature and ambient moisture levels to simulate possible industrial operating conditions, exhibiting good mechanical stability and integrity in pelletised materials and membranes. Additionally, the microporous structure of the three-dimensional MOF allowed us to study the adsorptive capacity of **1**, displaying almost negligible CO₂ uptake in the as-synthesised material. However, the solvent exchange procedure allowed a partial replacement of coordinated DMF molecules with ethanol, maintaining its structural stability and easing the material's activation by replacing a more volatile solvent. Consequently, sorption isotherms were repeated, exhibiting an uptake of 0.54 mmol/g. Finally, motivated by the known antibacterial capacity of the Cu²⁺

and 3,4-dihydroxybenzoic acid ligands, we decided to study the antibacterial activity of compound **1** and its precursors towards pathogenic *S. aureus* bacteria by the disk-diffusion method, exhibiting that the antibacterial activity of both the Cu^{2+} and 3,4-dihydroxybenzoic acid ligand remained practically unaltered after the formation of the compound.

Supplementary Materials: The following supporting information can be downloaded at: <https://www.mdpi.com/article/10.3390/molecules27228073/s1>, Table S1: Table of the continuous Shape Measurements for the CuO_5 coordination environment; Figure S1: View along *a*, *b* and *c* crystallographic axis, the corresponding topological representation and the view of “ABBA..” SBU; Table S2: Table of the continuous Shape Measurements for the CuO_6 coordination environment; Figure S2: Figure of TG/DTA analysis of as synthesised compound **1**; Figure S3: Figure of TG/DTA analysis of compound **1** performed after solvent exchange with EtOH during 16 h (left side) and experimental PXRD for complex **1** before and after solvent exchange with EtOH (right side); Table S3: Elemental analysis of compound **1**; Table S4: Selected bond lengths (in Å) and bond angles (in °) for the Cu^{2+} coordination environments present in $[\text{Cu}_3\text{L}_2(\text{DMF})_2]$ (**1**); Figure S4: Thermal evolution of as synthesised compound **1**; Figure S5: Comparison between the PXRD transformed phase of compound **1** obtained from thermal evolution at 190 °C and the phase obtained soaking compound **1** in H_2O during 16 h; Figure S6: Powder X-ray diffractograms of the studied materials, as-synthesized and after processing into pellets and membranes subsequent moisture treatment; Figure S7: Powder X-ray diffractograms of the studied materials, as-synthesized and after processing into pellets after temperature-cycles; Figure S8: Water adsorption isotherm of compound **1** as synthesised (AS) and after solvent-exchange with EtOH for 16 h; Figure S9: N_2 and CO_2 adsorption at desorption isotherms at 77 K and 273 K of **1**, upon outgassing at 170 °C for 6 h; Figure S10: Infrared spectra of the ligand and compound **1**; Figure S11: SEM images of compound **1**; Figure S12: Figure of the pattern matching analysis and experimental PXRD for complex **1**; Figure S13: Experimental PXRD for complexes **1** after being soaked for 16 h in several solvents. References [40–48] are cited in the supplementary materials.

Author Contributions: Conceptualisation, J.M.S. and A.R.-D.; methodology, E.E.-E., S.R., R.F.M.; software, V.K.A.-F.; validation, M.P.-M., P.B., F.A.A.P. and J.M.D.-L.; formal analysis, J.M.D.-L.; investigation, E.E.-E.; resources, M.P.-M., F.A.A.P., F.F. (Filipe Figueiredo), J.M.S. and A.R.-D.; data curation, P.B., S.R. and J.M.D.-L. and.; writing—original draft preparation, E.E.-E.; writing—review and editing, J.M.D.-L., J.M.S.; visualisation, A.R.-D.; supervision, S.R., F.F. (Flávio Figueira); project administration, J.M.S. and A.R.-D.; funding acquisition, J.M.S. and A.R.-D. All authors have read and agreed to the published version of the manuscript.

Funding: This work was developed within the scope of the projects given by the University of the Basque Country (GIU 20/028 Junta de Andalucía (B-FQM-734-UGR20, ProyExcel_00386 and FQM-394), the Spanish Ministry of Science, Innovation and Universities (MCIU/AEI/FEDER, UE) (PGC2018-102052-B-C21) and the CICECO–Aveiro Institute of Materials (UIDB/50011/2020 and UIDP/50011/2020).

Informed Consent Statement: Not applicable.

Data Availability Statement: The data that support the findings of this study are available from the corresponding author upon reasonable request.

Acknowledgments: E.E. is grateful to the Government of the Basque Country for the predoctoral fellowship and R.F.M for the Junior Research Position CEECIND/ 00553/2017. S.R. acknowledges the Juan de la Cierva Incorporación Fellowship (grant agreement no. IJC2019-038894-I). The authors thank for technical and human support provided by SGiker of UPV/EHU and European funding (ERDF and ESF) and also wish to acknowledge the terrific help of all reviewers of the present manuscript, whose comments helped to improve the quality of the work.

Conflicts of Interest: The authors declare no conflict of interest.

Sample Availability: Samples of the compounds ... are available from the authors.

References

1. Zhang, S.; Ye, J.; Liu, Z.; Lu, H.; Shi, S.; Qi, Y.; Ning, G. Superior antibacterial activity of Fe₃O₄@copper(II) metal-organic framework core-shell magnetic microspheres. *Dalton Trans.* **2020**, *49*, 13044–13051. [[CrossRef](#)] [[PubMed](#)]
2. Wyszogrodzka, G.; Marszałek, B.; Gil, B.; Doroczyński, P. Metal-organic frameworks: Mechanisms of antibacterial action and potential applications. *Drug Discov. Today* **2016**, *21*, 1009–1018. [[CrossRef](#)] [[PubMed](#)]
3. Feng, X.; Li, J.; Feng, Y.; Zhang, K.; Chen, N.; Fang, H.; Li, Z. Series of d10 complexes based on sulfamethoxazole: Auxiliary ligand induces structure diversity, luminescence and antibacterial properties. *J. Solid State Chem.* **2021**, *302*, 122351. [[CrossRef](#)]
4. Feng, X.; Xu, C.; Wang, Z.Q.; Tang, S.F.; Fu, W.J.; Ji, B.M.; Wang, L.Y. Aerobic oxidation of alcohols and the synthesis of benzoxazoles catalyzed by a cuprocupric coordination polymer (Cu⁺-CP) assisted by TEMPO. *Inorg. Chem.* **2015**, *54*, 2088–2090. [[CrossRef](#)] [[PubMed](#)]
5. López-Viseras, M.E.; Fernández, B.; Hilfiker, S.; González, C.S.; González, J.L.; Calahorra, A.J.; Colacio, E.; Rodríguez-Diéguez, A. *In vivo* potential antidiabetic activity of a novel zinc coordination compound based on 3-carboxy-pyrazole. *J. Inorg. Biochem.* **2014**, *131*, 64–67. [[CrossRef](#)]
6. Fernández, B.; Fernández, I.; Cepeda, J.; Medina-O'Donnell, M.; Rufino-Palomares, E.E.; Raya-Barón, Á.; Gómez-Ruiz, S.; Pérez-Jiménez, A.; Lupiáñez, J.A.; Reyes-Zurita, F.J.; et al. Modulating Anticancer Potential by Modifying the Structural Properties of a Family of Zinc Metal-Organic Chains Based on 4-Nitro-1H-pyrazole. *Cryst. Growth Des.* **2018**, *18*, 969–978. [[CrossRef](#)]
7. García-García, A.; Rojas, S.; Rivas-García, L.; Navarro-Hortal, M.D.; Romero-Márquez, J.M.; Fernández-Bolaños, J.G.; Choquesillo-Lazarte, D.; Salinas-Castillo, A.; López, Ó.; Quiles, J.L.; et al. A glyclazide complex based on palladium towards Alzheimer's disease: Promising protective activity against Aβ-induced toxicity in *C. elegans*. *Chem. Commun.* **2022**, *58*, 1514–1517. [[CrossRef](#)] [[PubMed](#)]
8. Navas, A.; Jannus, F.; Fernández, B.; Cepeda, J.; O'Donnell, M.M.; Díaz-Ruiz, L.; Sánchez-González, C.; Llopis, J.; Seco, J.M.; Rufino-Palomares, E.; et al. Designing single-molecule magnets as drugs with dual anti-inflammatory and anti-diabetic effects. *Int. J. Mol. Sci.* **2020**, *21*, 3146. [[CrossRef](#)] [[PubMed](#)]
9. Caballero, A.B.; Rodríguez-Diéguez, A.; Quirós, M.; Salas, J.M.; Huertas, Ó.; Ramírez-Macias, I.; Olmo, F.; Marín, C.; Chaves-Lemaur, G.; Gutierrez-Sánchez, R.; et al. Triazolopyrimidine compounds containing first-row transition metals and their activity against the neglected infectious Chagas disease and leishmaniasis. *Eur. J. Med. Chem.* **2014**, *85*, 526–534. [[CrossRef](#)] [[PubMed](#)]
10. Zhang, X.; Peng, F.; Wang, D. MOFs and MOF-Derived Materials for Antibacterial Application. *J. Funct. Biomater.* **2022**, *13*, 215. [[CrossRef](#)]
11. Jo, J.H.; Kim, H.-C.; Huh, S.; Kim, Y.; Lee, D.N. Antibacterial activities of Cu-MOFs containing glutarates and bipyridyl ligands. *Dalton Trans.* **2019**, *48*, 8084–8093. [[CrossRef](#)] [[PubMed](#)]
12. Seil, J.T.; Webster, T.J. Antimicrobial applications of nanotechnology: Methods and literature. *Int. J. Nanomed.* **2012**, *7*, 2767–2781. [[CrossRef](#)]
13. Seco, J.M.; Fairen-Jimenez, D.; Calahorra, A.J.; Méndez-Liñán, L.; Pérez-Mendoza, M.; Casati, N.; Colacio, E.; Rodríguez-Diéguez, A. Modular structure of a robust microporous MOF based on Cu₂ paddle-wheels with high CO₂ selectivity. *Chem. Commun.* **2013**, *49*, 11329–11331. [[CrossRef](#)] [[PubMed](#)]
14. Casey, A.L.; Adams, D.; Karpanen, T.J.; Lambert, P.A.; Cookson, B.D.; Nightingale, P.; Miruszenko, L.; Shillam, R.; Christian, P.; Elliott, T.S.J. Role of copper in reducing hospital environment contamination. *J. Hosp. Infect.* **2010**, *74*, 72–77. [[CrossRef](#)] [[PubMed](#)]
15. Santo, C.E.; Quaranta, D.; Grass, G. Antimicrobial metallic copper surfaces kill *Staphylococcus haemolyticus* via membrane damage. *Microbiologyopen* **2012**, *1*, 46–52. [[CrossRef](#)] [[PubMed](#)]
16. Díaz-García, D.; Ardiles, P.R.; Prashar, S.; Rodríguez-Diéguez, A.; Páez, P.L.; Gómez-Ruiz, S. Preparation and Study of the Antibacterial Applications and Oxidative Stress Induction of Copper Maleamate-Functionalized Mesoporous Silica Nanoparticles. *Pharmaceutics* **2019**, *11*, 30. [[CrossRef](#)] [[PubMed](#)]
17. Lamichhane, J.R.; Osdaghi, E.; Behlau, F.; Köhl, J.; Jones, J.B.; Aubertot, J.N. Thirteen decades of antimicrobial copper compounds applied in agriculture. A review. *Agron. Sustain. Dev.* **2018**, *38*, 28. [[CrossRef](#)]
18. Chiericcatti, C.; Basilico, J.C.; Zapata Basilico, M.L.; Zamaro, J.M. Novel application of HKUST-1 metal-organic framework as antifungal: Biological tests and physicochemical characterizations. *Microporous Mesoporous Mater.* **2012**, *162*, 60–63. [[CrossRef](#)]
19. Abbasi, A.R.; Akhbari, K.; Morsali, A. Dense coating of surface mounted CuBTC Metal-Organic Framework nanostructures on silk fibers, prepared by layer-by-layer method under ultrasound irradiation with antibacterial activity. *Ultrason. Sonochem.* **2012**, *19*, 846–852. [[CrossRef](#)]
20. Rodríguez, H.S.; Hinestroza, J.P.; Ochoa-Puentes, C.; Sierra, C.A.; Soto, C.Y. Antibacterial activity against *Escherichia coli* of Cu-BTC (MOF-199) metal-organic framework immobilized onto cellulosic fibers. *J. Appl. Polym. Sci.* **2014**, *131*, 40815. [[CrossRef](#)]
21. Wang, C.; Qian, X.; An, X. In situ green preparation and antibacterial activity of copper-based metal-organic frameworks/cellulose fibers (HKUST-1/CF) composite. *Cellulose* **2015**, *22*, 3789–3797. [[CrossRef](#)]
22. Ren, J.; Langmi, H.W.; North, B.C.; Mathe, M. Review on processing of metal-organic framework (MOF) materials towards system integration for hydrogen storage. *Int. J. Energy Res.* **2015**, *39*, 607–620. [[CrossRef](#)]
23. Yuan, J.; Li, J.; Che, S.; Li, G.; Liu, X.; Sun, X.; Zou, L.; Zhang, L.; Liu, Y. Two unique copper cluster-based metal-organic frameworks with high performance for CO₂ adsorption and separation. *Inorg. Chem. Front.* **2019**, *6*, 556–561. [[CrossRef](#)]
24. Rubio-Martinez, M.; Avci-Camur, C.; Thornton, A.W.; Imaz, I.; Maspoch, D.; Hill, M.R. New synthetic routes towards MOF production at scale. *Chem. Soc. Rev.* **2017**, *46*, 3453–3480. [[CrossRef](#)] [[PubMed](#)]

25. Valizadeh, B.; Nguyen, T.N.; Stylianou, K.C. Shape engineering of metal–organic frameworks. *Polyhedron* **2018**, *145*, 1–15. [[CrossRef](#)]
26. Ma, Q.; Zhang, T.; Wang, B. Shaping of metal-organic frameworks, a critical step toward industrial applications. *Matter* **2022**, *5*, 1070–1091. [[CrossRef](#)]
27. Ntouros, V.; Kousis, I.; Pisello, A.L.; Assimakopoulos, M.N. Binding Materials for MOF Monolith Shaping Processes: A Review towards Real Life Application. *Energies* **2022**, *15*, 1489. [[CrossRef](#)]
28. Figueira, F.; Mendes, R.F.; Domingues, E.M.; Barbosa, P.; Figueiredo, F.; Paz, F.A.A.; Rocha, J. Easy processing of metal-organic frameworks into pellets and membranes. *Appl. Sci.* **2020**, *10*, 798. [[CrossRef](#)]
29. Ghanbari, T.; Abnisa, F.; Wan Daud, W.M.A. A review on production of metal organic frameworks (MOF) for CO₂ adsorption. *Sci. Total Environ.* **2020**, *707*, 135090. [[CrossRef](#)]
30. Nofrizal; Putra, D.P.; Arbain, D. Antioxidant and antibacterial constituents from two Sumatran ferns, *Trichomanes javanicum* and *Oleandra pistillaris*. *Nat. Prod. Commun.* **2017**, *12*, 1263–1264. [[CrossRef](#)]
31. Llunell, M.; Casanova, D.; Cirera, J.; Bofill, J.M.; Alemany, P.; Alvarez, S.; Pinsky, M.; Avnir, D. *Program for the Stereochemical Analysis of Molecular Fragments by Means of Continuous Shape Measures and Associated Tools*; SHAPE, v1.1b; University of Barcelona: Barcelona, Spain, 2005; pp. 1–35.
32. Blatov, V.A.; Shevchenko, A.P.; Proserpio, D.M. Applied topological analysis of crystal structures with the program package topopro. *Cryst. Growth Des.* **2014**, *14*, 3576–3586. [[CrossRef](#)]
33. Spek, A.L. Structure validation in chemical crystallography. *Acta Crystallogr. Sect. D Biol. Crystallogr.* **2009**, *65*, 148–155. [[CrossRef](#)] [[PubMed](#)]
34. Dang, L.L.; Zong, D.X.; Lu, X.Y.; Zhang, T.T.; Chen, T.; Sun, J.L.; Zhao, J.Z.; Liu, M.Y.; Liu, S.R. The Selective CO₂ Adsorption and Photothermal Conversion Study of an Azo-Based Cobalt-MOF Material. *Molecules* **2022**, *27*, 6873. [[CrossRef](#)] [[PubMed](#)]
35. Gü Ç Lü, Y.; Erer, H.; Demiral, H.; Altintas, C.; Keskin, S.; Tumanov, N.; Su, B.-L.; Semerci, F. Oxalamide-Functionalized Metal Organic Frameworks for CO₂ Adsorption. *Cite This ACS Appl. Mater. Interfaces* **2021**, *13*, 33198. [[CrossRef](#)]
36. Bae, Y.S.; Farha, O.K.; Spokoyny, A.M.; Mirkin, C.A.; Hupp, J.T.; Snurr, R.Q. Carborane-based metal–organic frameworks as highly selective sorbents for CO₂ over methane. *Chem. Commun.* **2008**, *9*, 4135–4137. [[CrossRef](#)] [[PubMed](#)]
37. Lowy, F.D. Staphylococcus aureus infections. *N. Engl. J. Med.* **1998**, *339*, 520–532. [[CrossRef](#)] [[PubMed](#)]
38. Lee, D.N.; Kim, Y.R.; Yang, S.; Tran, N.M.; Park, B.J.; Lee, S.J.; Kim, Y.; Yoo, H.; Kim, S.J.; Shin, J.H. Controllable Nitric Oxide Storage and Release in Cu-BTC: Crystallographic Insights and Bioactivity. *Int. J. Mol. Sci.* **2022**, *23*, 9098. [[CrossRef](#)]
39. O'Brien, F.E. The Control of Humidity by Saturated Salt Solutions. *J. Sci. Instrum.* **1948**, *25*, 73–76. [[CrossRef](#)]
40. Rodríguez-Carvajal, J. *Fullprof*; Version 2.5d; Université Paris-Saclay: Paris, France, 2000.
41. Kottke, T.; Stalke, D. Crystal handling at low temperatures. *J. Appl. Cryst.* **1993**, *26*, 615–619. [[CrossRef](#)]
42. *SAINt+*, *Data Integration Engine, V. 8.37a*©; Bruker AXS: Madison, WI, USA, 1997–2015.
43. Krause, L.; Herbst-Irmer, R.; Sheldrick, G.M.; Stalke, D. Comparison of silver and molybdenum microfocus X-ray sources for single-crystal structure determination. *J. Appl. Crystallogr.* **2015**, *48*, 3–10. [[CrossRef](#)]
44. Sheldrick, G.M. *SADABS User Manual*; SADABS; University of Göttingen: Göttingen, Germany, 2008.
45. Sheldrick, G.M. SHELXT-Integrated space-group and crystal-structure determination. *Acta Crystallogr. Sect. A Found. Crystallogr.* **2015**, *71*, 3–8. [[CrossRef](#)]
46. Hübschle, C.B.; Sheldrick, G.M.; Dittrich, B. ShelXle: A Qt graphical user interface for SHELXL. *J. Appl. Cryst.* **2011**, *44*, 1281–1284. [[CrossRef](#)] [[PubMed](#)]
47. Brandenburg, K. *DIAMOND*; Version 3.2f; Crystal Impact GbR: Bonn, Germany, 1997–2010.
48. Liu, X.M.; Xie, L.H.; Wu, Y. Recent advances in the shaping of metal–organic frameworks. *Inorg. Chem. Front.* **2020**, *7*, 2840–2866. [[CrossRef](#)]